A Further Study of ENSO Rectification: Results from an OGCM with a Seasonal Cycle*

LIJUAN HUA

State Key Laboratory of Numerical Modeling for Atmospheric Sciences and Geophysical Fluid Dynamics (LASG), Institute of Atmospheric Physics, Chinese Academy of Sciences, and College of Earth Science, University of Chinese Academy of Sciences, Beijing, China

YONGQIANG YU

State Key Laboratory of Numerical Modeling for Atmospheric Sciences and Geophysical Fluid Dynamics (LASG), Institute of Atmospheric Physics, Chinese Academy of Sciences, Beijing, China

DE-ZHENG SUN

Cooperative Institute for Research in Environmental Sciences, University of Colorado and NOAA/ESRL, Boulder, Colorado

(Manuscript received 7 June 2014, in final form 7 October 2014)

ABSTRACT

The potential role that rectification of ENSO plays as a viable mechanism to generate climate anomalies on the decadal and longer time scales demands a thorough study of this process. In this paper, rectification of ENSO was studied using an ocean GCM that has a realistic seasonal cycle. In addition to conducting a pair of forced ocean GCM experiments with and without ENSO fluctuations, as done in a previous study, a forced experiment was also conducted with the sign of wind anomalies reversed, with the goal of clarifying the role of the asymmetry in the wind forcing and more generally to better understand the nonlinear dynamics responsible for the rectification. It is found that the rectification effect of ENSO is to cool the western Pacific warm pool and warm the eastern equatorial Pacific. Further, it is found that when the sign of the wind stress anomalies is reversed the impact of the rectification on the mean state remains almost unchanged. This lack of change is further explained by noting that the upper-ocean temperature and velocity anomalies (T', u', v', and w') are found to respond to the wind stress anomalies linearly, except for the strongest El Niño years. Thus, the correlation between T' and (u', v', w') [and thus the nonlinear dynamical heating (NDH)] remains the same when the sign of the wind stress anomalies is reversed. Indeed, the spatial patterns of NDH in all four seasons are found to resemble the rectified effect of ENSO in the mean temperature field in the respective seasons, indicating the critical role of NDH in the rectification.

1. Introduction

Since Bjerknes (1969) linked El Niño to the large-scale air–sea interaction in the tropical Pacific,

El Niño–Southern Oscillation (ENSO) has been extensively studied. Many aspects of ENSO dynamics have been understood. For example, the rapid growth of an ENSO SST anomaly is linked to a positive feedback loop among SST, the surface winds, and ocean dynamics (Bjerknes 1969). The transition between an El Niño event and a La Niña event has been associated with a linear oscillator that involves the upper-ocean dynamics: the delayed oscillator (Suarez and Schopf 1988; Battisti and Hirst 1989), which emphasizes the reflection of the equatorial waves, and the recharge–discharge oscillator (Jin 1997), which underscores more the importance of the subsurface heat content. Attempting to

understand the birth of ENSO in the framework of a dynamical system, Sun (1997) linked ENSO to a nonlinear response of the coupled system to the intensity of the tropical heating, raising a potential role for ENSO events in the long-term heat balance of the tropical Pacific.

The role of the ENSO events in the long-term heat balance of the tropical Pacific and more generally the question regarding the time-mean effect of ENSO was picked up in the study of Sun (2003), Sun et al. (2004), and Sun and Zhang (2006). They conducted numerical experiments to illustrate that the response in the upper-ocean temperature to an increase in the tropical radiative heating is much different between the cases with ENSO than without ENSO. They suggested that the time-mean effect of ENSO is to cool the western Pacific warm pool and warm the subsurface thermocline water as well as the surface water of the tropical eastern ocean. Using a more sophisticated model, Yu and Sun (2009) also found that in response to perturbations in the extratropical region, the changes in the time-mean structure of the equatorial upper ocean are very different between the case in which ocean–atmosphere system is coupled over the equatorial region and the case where it is decoupled.

To delineate the time-mean effect of ENSO events more clearly, Liang et al. (2012) employed another approach: they quantified the time-mean effect of ENSO by contrasting the equilibrium state of the coupled tropical ocean–atmosphere with the actual realized climatology. At the equilibrium state of the coupled tropical ocean–atmosphere system, ENSO as an instability has not manifested while in the actual realized climatology ENSO has manifested. Thus, the difference between the two is a good measure of the ENSO effect in the climatology. Indeed, they have succeeded in doing such analysis with the use of an analytical model. The model is a highly simplified representation of the coupled tropical ocean–atmosphere system, but it encapsulates the major physics of the ENSO system. In the context of this model, they show unambiguously that the time-mean effect of ENSO is a warming to the eastern tropical Pacific (see Fig. 2), supporting the earlier results of Sun (2003) and Sun and Zhang (2006) as well as the earlier inference made from the ENSO asymmetry (Jin et al. 2003; Rodgers et al. 2004; Schopf and Burgman 2006). Liang et al. (2012) have also noted a correspondence between the degree of asymmetry of ENSO and its time-mean effect in the nonlinear box model for the tropical Pacific, but they show that this correspondence occurs not because the former causes the latter but because they are both caused by the nonlinear term in the heat budget equation. Note that although the

asymmetry of ENSO was first suggested as a mechanism for the time-mean effect of ENSO events, the asymmetry alone is not a sufficient condition for a significant time-mean (or rectification) effect of ENSO because such a residual effect will depend quantitatively on how one defines El Niño and La Niño events.

The simplicity of the model used by Liang et al. (2012), however, does not give the corresponding meridional structure of the warming, limiting the full application of the mechanism revealed in that model to the observed decadal warming. Sun et al. (2014, hereinafter SZ2014) then employed another methodology to delineate the effect of ENSO events on the time-mean state of the equatorial upper ocean. This new method consists of contrasting the time-mean state of two forced ocean GCM experiments. In one experiment, the long-term-mean surface wind stress is used while in the other the surface wind stress has interannual fluctuations. The two runs have identical long-term-mean surface wind stress. The two runs are also restored to the same prescribed SST. Thus, the thermal boundary conditions are such that they will damp any differences between the model and prescribed SSTs resulting from the differences in the variance in the surface winds through upper-ocean dynamics in these two experiments. By having more realistic ENSO events in the simulation and the use of a GCM to provide the spatial structure of the time-mean effect of ENSO events, this new methodology compliments the earlier strategies—examining the response of the mean climate to a perturbation to the heat budget of the tropical Pacific using a coupled model (Sun 2003; Sun and Zhang 2006)—and the method of differencing the time-mean state from the equilibrium state of the tropical Pacific using an analytical model (Liang et al. 2012).

The present study uses a more sophisticated ocean model in order to find out whether SZ2014's results are dependent on the specific ocean model used. Also, the present model has a realistic seasonal cycle, which allows one to address specifically whether the results of SZ2014 will be seasonally dependent. In addition, SZ2014 do not quantify the relative contribution of the asymmetry of wind stress and nonlinear ocean dynamics to the rectification. To demonstrate the critical role of upper-ocean dynamics, we introduce a new idealized experiment to facilitate understanding, in which the interannual monthly anomalies are reversed so that the contribution of the asymmetry of wind stress to ENSO dynamics can be isolated. Consequently, the mechanism of the rectification will be delineated in greater detail. The paper is organized as follows: Section 2 introduces the methodology. Section 3 presents the main results. Conclusions are provided in section 4.

In addition to the line of research we have just reviewed above and will follow in the present study, there are also more empirically based studies of the time-mean effect of ENSO. For example, Rodgers et al. (2004) found in a long simulation by a coupled GCM that changes in the mean state between decades with high ENSO activity and decades with low ENSO activity resemble the residual of the two phases of ENSO in the model. They thereby suggested that the asymmetry could be a mechanism for decadal changes in the tropical Pacific SST. Noting a 15-yr cycle in the level of ENSO activity in an extended SST dataset consisting of historical and paleoclimate data and a change in the asymmetry of ENSO with this decadal cycle, Sun and Yu (2009) have argued that the residual effect from the ENSO asymmetry may provide an explanation for the decadal cycle they have noted in the level of ENSO activity. Yu and Kim (2011) have further investigated the decadal variability in CMIP3 models from the angle of ENSO asymmetry. These studies are descriptive and, as we have remarked, the asymmetry of ENSO by itself does not necessarily imply a significant time-mean effect. More recently, an analysis of the tropical Pacific decadal variability in a 2000-yr integration with the Geophysical Fluid Dynamics Laboratory Climate Model (Delworth et al. 2006; Wittenberg 2009) was conducted by Ogata et al. (2013). They found that ENSO amplitude modulation is highly correlated with the second EOF mode of tropical Pacific decadal variability, which suggests that the rectified effect of ENSO is significant.

Understanding the time-mean effect of ENSO is important to understand decadal climate changes in the tropical Pacific including the decadal modulation of ENSO variance (Liang et al. 2012; Ogata et al. 2013; SZ2014). As global warming as expressed in surface temperatures is experiencing a hiatus and this hiatus may be linked to the decadal shift in the state of the tropical Pacific (Kosaka and Xie 2013; Meehl et al. 2013), the need to thoroughly assess the time-mean effect of ENSO has become even more apparent.

2. Methodology

a. Model description

The OGCM used in this study is a primitive equation ocean model developed at the State Key Laboratory of Numerical Modeling for Atmospheric Sciences and Geophysical Fluid Dynamics (LASG), Institute of Atmospheric Physics (IAP) in Beijing, China. It is called the LASG IAP Climate Ocean Model (LICOM; Liu et al. 2004b, 2012; Yu et al. 2011). It is a distinctly new model and is built using the Arakawa B grid. LICOM

has been widely applied in studying air–sea interaction and climate change simulations, and it has been shown to be able to simulate realistically the large-sale patterns of oceanic circulation (Liu et al. 2004a; Yu et al. 2007, 2008, 2011).

The version of the model we used is LICOM2.0, which includes some new parameterization schemes, such as a new turbulent mixing scheme (Canuto and Dubovikov 2005), solar radiation penetration, and an improved isopycnal mixing scheme (Gent and McWilliams 1990; Large et al. 1997). In addition, both horizontal and vertical resolutions are enhanced for the upper ocean of LICOM2.0. It is a global ocean model that covers from 75°S to 88°N (the North Pole is treated as an isolated island). In particular, the horizontal resolution is 1° × 1° but the meridional resolution is increased to 0.5° between 10°S and 10°N, and there are 30 layers with 15 equal-depth levels in the upper 150 m. Using climatological monthly-mean wind stress data from the Ocean Model Intercomparison Project (OMIP; Roeske 2001) (which are based on the European Centre for Medium-Range Weather Forecasts reanalysis; Gibson et al. 1997), LICOM2.0 was first integrated from a state without motion to a statistical equilibrium state through a 500-yr spinup. The end state of year 500 is then used as the initial state for the numerical experiments that will be described below.

b. Experiment design

To evaluate the model's ability to simulate ENSO variability and to further understand the rectification effect of ENSO events onto the climate-mean state in the upper Pacific ocean on the decadal and longer time scales, one control and two sensitivity runs are designed. The control run has been integrated for 44 yr with climatological winds as the surface wind stress applied on the ocean and with sea surface temperature and salinity being restored to the Levitus94 datasets (Levitus and Boyer 1994; Levitus et al. 1994) as described by Liu et al. (2004a). Using the restoring thermal boundary condition allows us to underscore the importance of the subsurface ocean dynamics in the rectification of ENSO. Indeed, as found in SZ2014 and will be shown in our results as well, the rectification effect of ENSO shows up in the subsurface and to a lesser degree in the surface when this restrictive boundary condition is used. In a way, it is a first step to get a conservative estimate of the rectified effect of ENSO.

In those two sensitivity runs, the surface wind stresses are climatological winds plus the interannual monthly anomalies, and the surface boundary conditions for temperature and salinity are kept as control run. In the first sensitivity run (referred to as WSA), which is same

as the sensitivity run in SZ2014, the interannual monthly anomalies of 1958–2001 from the 40-yr European Centre for Medium-Range Weather Forecasts Re-Analysis (ERA-40; Uppala et al. 2005) over the tropical Pacific (30°S–30°N, 120°E–80°W) are superimposed on the climatological surface wind stress. The second sensitivity run (referred to as WSA_R) is the same as WSA, except the signs of the interannual monthly anomalies are reversed. It is important to note that, because of the restoring boundary conditions, the simulated surface temperature and salinity are restored to the climatological-mean value with seasonal cycle. Then, as a negative feedback, the restoring boundary conditions would have a damping effect on any perturbations of sea surface temperature and salinity deviated from the climatological-mean state. Consequently, the SST anomalies in the run could only result from the wind stress forcing or the ocean dynamics.

As we already mentioned in the introduction, the time-mean effect of ENSO delineated in SZ2014 may come from by two factors: the asymmetry of wind stress forcing or the internal dynamical process in the ocean. The comparison between those two sensitivity runs WSA and WSA_R may help quantify the relative contribution of wind stress forcing and ocean dynamics to the time-mean effect of ENSO.

3. Results

In this section, we will first show that the observed ENSO variability is well simulated by the model (section 3a). We then contrast the experiments with ENSO (WSA) and that without ENSO to delineate the time-mean effect of ENSO. The differences will be presented as function of seasons. In addition to calculating the NDH for understanding this time-mean effect of ENSO, we also contrast the run in which the ENSO forcing is reversed (WSA_R) with that run without ENSO (control run). One surprising result we will present is that reversing ENSO in the surface forcing does not seem to alter significantly the time-mean effect. We will show that this is because the responses of the current and temperature anomalies to the ENSO fluctuations in the surface forcing are largely linear, and thus the correlation between the velocity and temperature anomalies remains the same regardless of the sign of the ENSO anomaly in the surface winds. The results underscore a fundamental role of the west–east asymmetry in the equilibrium state in the Pacific that is established even in the absence of the ENSO fluctuations (section 3b).

a. Simulated mean state and ENSO variability

Climatological-mean SST averaged over the whole 44 yr from WSA run are shown in Fig. 1b. The figure

indicates that the ocean model can reproduce the observed large-scale spatial pattern of SST (Fig. 1a). Some differences between the model simulations and the observations are found in the western warm-pool region: in particular, in the region between 120° and 140°E along the equator, where the simulated SST is 1°C higher than observed. In the cold-tongue region of the central and eastern equatorial Pacific, the simulated SST is 1°C lower than observations. The cold tongue extends a little farther west. In addition, significant warm bias up to 1°C in SST is also found in the southeast coast. These biases are very common model biases for almost all the state-of-the-art OGCMs (Sun et al. 2009). Figures 1c and 1d show the temperature and zonal current in the equatorial upper ocean from observations and the model. The figure shows that the basic structure of the observed equatorial thermocline is well simulated by the model although the simulated thermocline around 120°E is a little deeper than observed and the maximum strength of the equatorial undercurrent is somewhat weaker.

Figure 2 shows the seasonal cycle in equatorial SST (shown as deviations from the annual-mean temperature). The variation in the simulated SST is dominated by the annual harmonic that peaks at about 100°W, with the warmest SST reached in March and the coldest SST reached in September. These features agree well with the observations. The seasonal variations in the eastern equatorial Pacific are in contrast to the seasonal variations in the western Pacific, where a semiannual cycle of SST is the most pronounced signal on the equator.

The observed ENSO variability is well simulated by the OGCM as shown in Fig. S1 of the supplementary material, which compares the time series of the Niño-3 SST from observations (Rayner et al. 2003) with that from the forced ocean GCM run WSA. The two time series are almost identical. All the observed El Niño and La Niño events are captured by the model simulations. The two time series have a correlation 0.83 with each other. Note this is higher than the correlation in SZ2014, which is 0.75. The present model has more improvement in simulating the timing—the onset and termination of El Niño events—but the simulated amplitude is still weaker. This discrepancy is expected given that the thermal boundary condition is simplified and the sea surface temperature being restored to the observed climatological datasets (Levitus and Boyer 1994; Levitus et al. 1994). The standard deviation of Niño-3 (5°N–5°S, 150°–90°W) index from observations and WSA are 0.88° and 0.58°C, respectively, and the simulated variability in magnitude is lower than that in SZ2014 (0.79°C). This can be attributed to the experimental design as stated above. Recall that, in SZ2014, the restoring SST is zonally uniform and has the value of warm-pool SST.
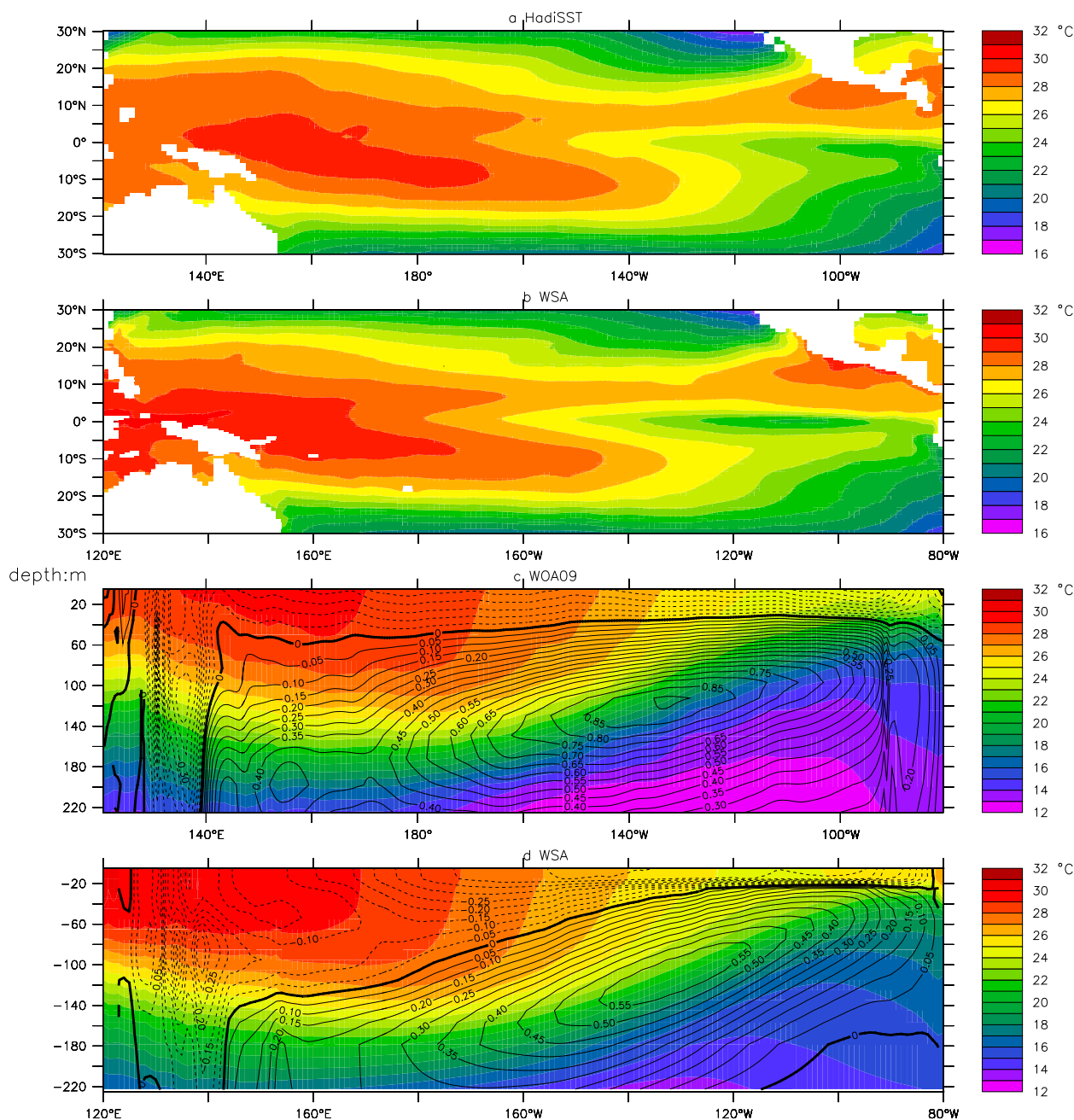
FIG. 1. Climatological SST distribution in the tropical Pacific from (a) observations (Rayner et al. 2003) and (b) WSA. Temperature in the equatorial upper ocean (5°N–5°S) as a function of longitude and depth from (c) *World Ocean Atlas 2009* (*WOA09*; Locarnini et al. 2010) and (d) WSA. The contours are the time-mean equatorial undercurrent (EUC) (m s^{-1}).

The boundary condition in SZ2014 is based on the theoretical result in Sun (1997) that a zonally uniform SST—a warm pool extending all the way to the eastern Pacific—is an equilibrium solution of the system. The skewness of the Niño-3 index from observations and WSA are 0.98 and 0.48. The probability density functions (PDFs) for the Niño-3 SST of observations and WSA are further shown in Figs. S1b,c. The positive

skewness in the distribution is evident in both PDFs, although the extreme warm SST anomalies are 1.75°–2°C while the observations are 3.25°–3.5°C. This is because the variability is generally weak as evident in Fig. S1a.

The composites of the warm and cold phase SST anomalies are shown in Fig. S2 of the supplementary material together with their residuals as another
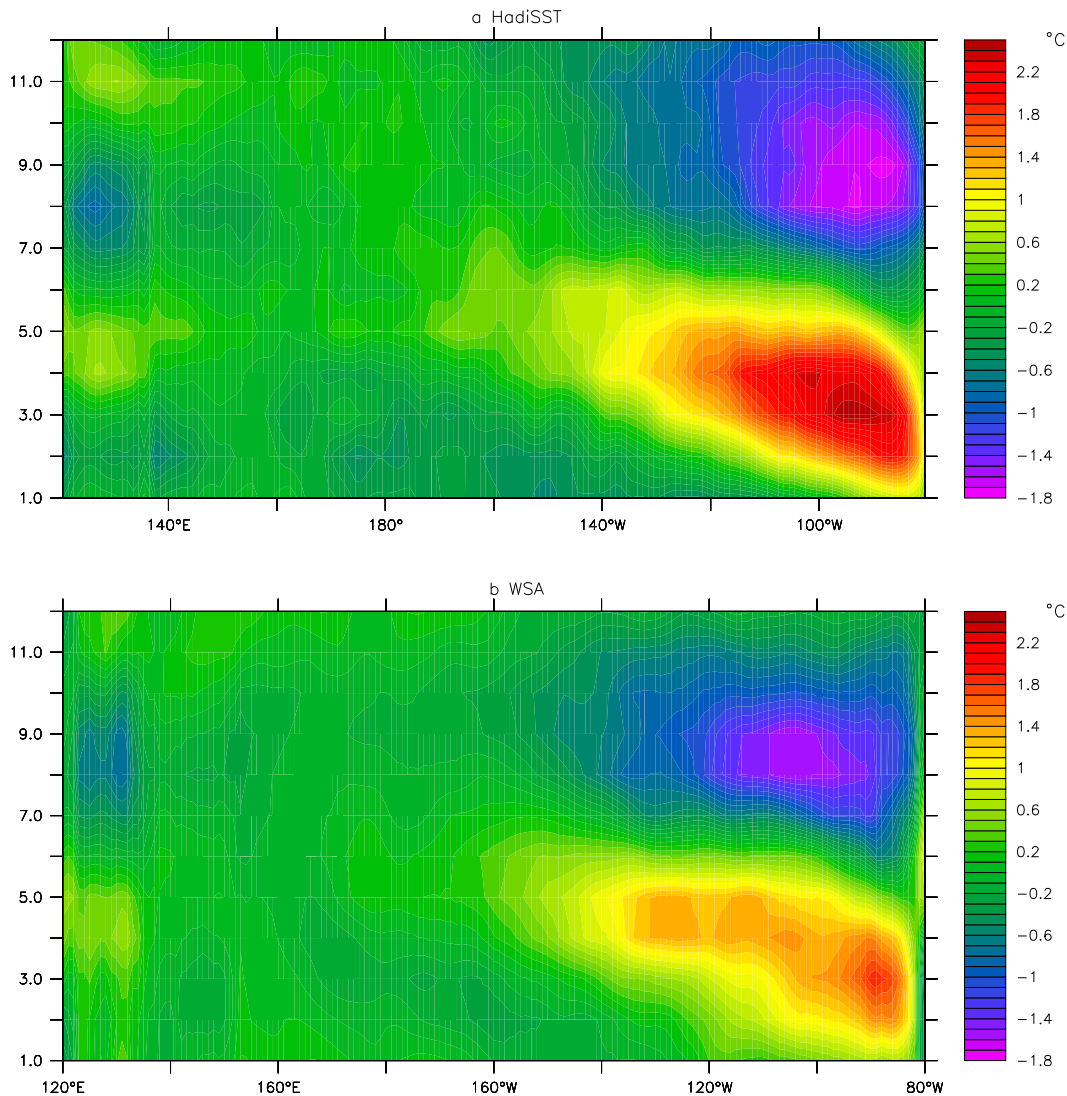
FIG. 2. The seasonal cycle in equatorial SST (5°N–5°S) from (a) observations (Rayner et al. 2003) and (b) WSA. Presented are the deviations from their respective annual mean SSTs.

measure of the ENSO asymmetry. Figure S2 provides the surface condition, in which the selected El Niño events are estimated as the 100 warmest months for the Niño-3 region and likewise the chosen La Niño events are from the 100 coldest months for the Niño-3 region. In this way, we can gain the same amount of both events; thus, the composite analysis can be more reasonable. The method is different from SZ2014, in which a 0.5°C threshold value for the monthly SST anomaly was used for obtaining the warm/cold events. The major characteristic of the spatial pattern of the SST anomalies are well simulated in the warm/cold phase as well as in the residual. Our model captures the major pattern of the observed asymmetry, implying that the ocean model has enough ability to reproduce ENSO asymmetry and can

be used as an effective tool to explore time-mean effect of ENSO and its physical mechanism. Comparing the results with SZ2014, the main discrepancy in the present model is in the warm phase. In the present model, the positive SST anomalies occur in the region of 15°–20°N, 160°–130°W while they agree more with observations in SZ2014. The differences are expected given the difference in the models.

Figure S3 in the supplementary material shows the corresponding subsurface features from the OGCM and the observations (Carton and Giese 2008). The major features of the spatial pattern of the temperature anomalies are well simulated in the warm/cold phase as well as in the residual. The model underestimates the positive temperature anomalies in the eastern Pacific

subsurface in the warm phase, which is the main cause of the underestimate of the warming in the residual. In SZ2014, the warming in the eastern Pacific subsurface is also less significant than observations in the residual. Furthermore, the cooling in the residual in the western Pacific subsurface is less significant than observations in SZ2014, and the present model captures the cooling signatures better than SZ2014.

Some differences between the simulation by the present OGCM and that used by SZ2014 are expected. First, the present OGCM is a global model. Second, resolution in the present model over the equator is somewhat lower than that used by SZ2014 (they used the NCAR Pacific basin model; Gent and Cane 1989). Fine equatorial resolution is important for simulating tropical instability waves (TIWs), which have been shown to be important contributors to the heating of the equatorial cold tongue (An 2008). Finally, the present model has the seasonal cycle in the wind stress applied. When the WSA run was redone with wind stress that has no seasonal cycle (i.e., long-term annual mean), we indeed find that the negative SST anomalies occur in the region of 15°–20°N, 160°–130°W, as in SZ2014. The residual cold anomalies are also weaker, resembling more the corresponding result from SZ2014.

These differences between the two models, while within the typical range of intermodel differences seen in state-of-the-art ocean models, provide an opportunity to examine whether the rectification found in SZ2014 is model dependent.

In Fig. S4 of the supplementary material, we further present the current anomalies together with available data from TAO. The simulated temporal evolution of the current anomalies is close to observations although the amplitude is a little smaller (Figs. S4a,b). Note that there are uncertainties in the wind stress used. The relatively low resolution of the ocean GCM could also contribute to the underestimate the magnitude of the current anomalies. Furthermore, we do not have enough data from TAO to cover the entire period of our simulation. The model–observation discrepancies appear to be more pronounced in the surface than the subsurface, suggesting that accurate representation of mixing in the surface boundary layer in the models remains a challenge.

b. Time-mean effect of ENSO

1) SIMULATIONS FROM WSA

As done in SZ2014, Fig. 3 presents the time-mean (1958–2001) upper-ocean temperature (Fig. 3a) and SST differences (Fig. 3b) between the run with ENSO (WSA) and the run without ENSO (control). Again, we find that, in the presence of ENSO, we have a cooler

western Pacific warm pool and a warmer eastern Pacific cold tongue. The central equatorial Pacific is also considerably warmer, a feature that also shows up in SZ2014. While the major pattern for the rectified effect of ENSO as shown by the present model is the same as SZ2014, there are some differences. For example, the warming center in the eastern equatorial Pacific is located at 100°–80°W and 30–80 m, but at 100°–80°W and 50–90 m in SZ2014. In particular, at 160°–120°W and 0–50 m, a warming is shown in SZ2014 but cooling is found in our model. In addition, temperature near the surface between 110° and 90°W is decreased in SZ2014 because of the presence of ENSO while in the present model temperature is increased. The extreme warming in SST occurs in the region 10°S–0°, 100°–90°W in the present model, which agrees with that in SZ2014, but another warming SST center in the southeastern Pacific in SZ2014 is not pronounced in the paper: the warming zone in SST along 5°N or 5°S in the central Pacific found in SZ2014 is not found here. Although there are some differences between the different models, the overall pattern in Fig. 3 resembles closely that in SZ2014. Our additional experiments suggest that these differences are not due to the seasonal cycle but a consequence of differences in other aspects of the two models.

The seasonal characteristics of ENSO variability in the model SZ2014 used are absent, but our model has. The time-mean temperature differences between simulations with ENSO (WSA) and without ENSO (control) during four seasons are shown in Fig. 4. The pattern for all seasons resembles Fig. 3a with the warming center occurring between 100° and 80°W at 30–80 m and the cooling center between 140°E and 180° at 100–140 m. Despite the spatial pattern in four seasons being similar, the amplitude of temperature changes varies significantly with seasons. For example, the most obvious warming located at the eastern equatorial Pacific arises in March–May (MAM), and the most significant cooling in the western equatorial Pacific occurs in December–February (DJF).

Figure S5 in the supplementary material further presents the corresponding surface features for the four seasons. The major spatial features follow Fig. 3b closely. The warming center is found in the region 110°–90°W and in the eastern boundary 90°–80°W, whereas the cooling center is found near the equator at 140°–160°E. There are significant differences across the different seasons. For example, the most significant warming in the eastern Pacific takes place in June–August (JJA), whereas the strongest cooling in the western Pacific is found in September–November (SON).

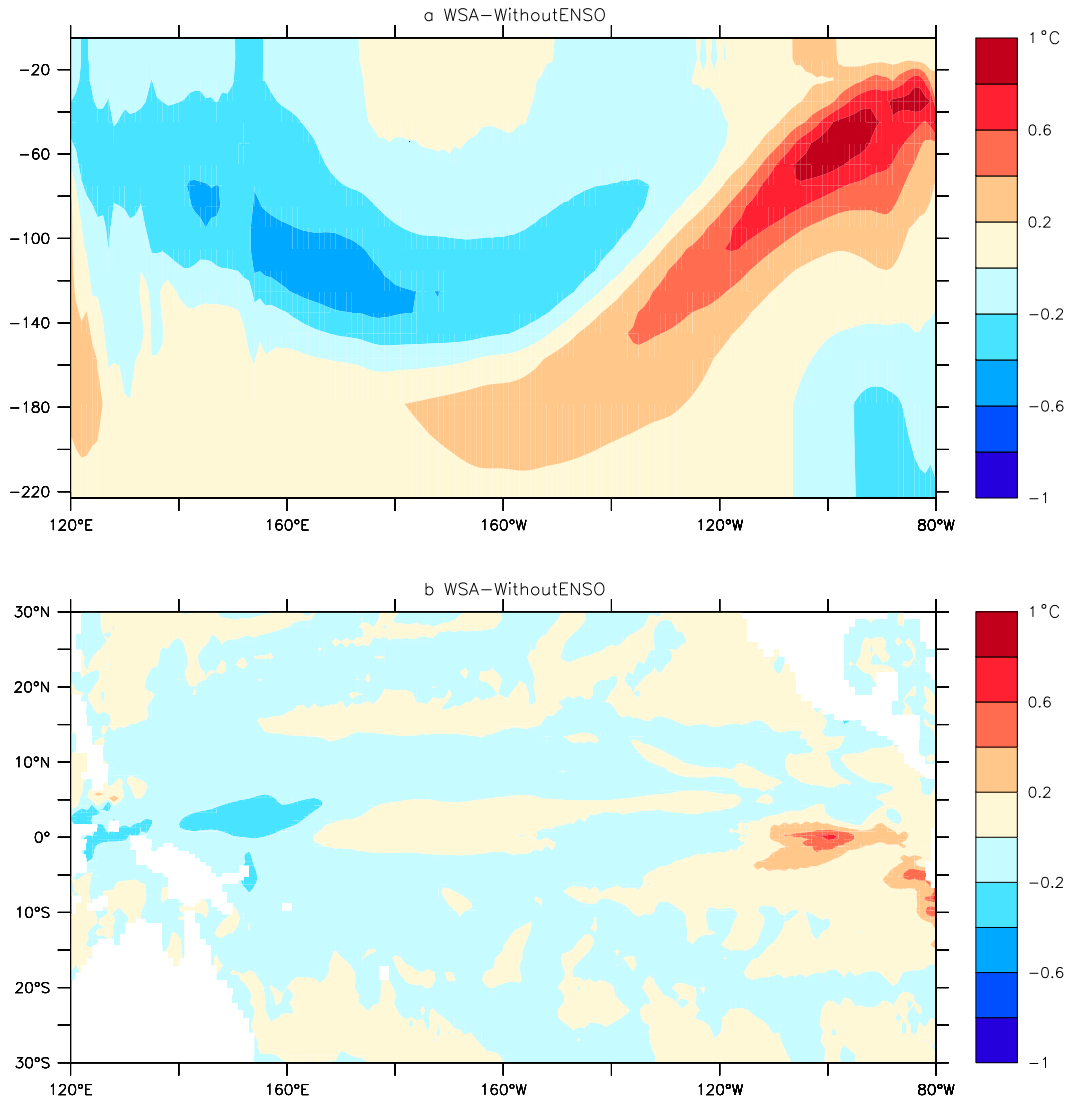An important suggestion from Liang et al. (2012) is that both ENSO asymmetry and its time-mean effect are

FIG. 3. Differences in the time-mean equatorial (a) upper-ocean temperature (5°N–5°S) and (b) SST between the runs with ENSO (WSA) and without ENSO (control).

caused by the nonlinear dynamical process. As many previous papers (Jin et al. 2003; An and Jin 2004) proposed, the nonlinear dynamical heating (NDH) starts from the following SST equation for the heat budget [heat flux and subgrid-scale contributions (e.g., heat diffusion, heat flux due to tropical instability wave) are attributed to the term R']:

$$\frac{\partial T'}{\partial t} = -(u'\partial x \overline{T} + v'\partial y \overline{T} + w'\partial z \overline{T} + \overline{u}\partial x T' + \overline{v}\partial y T' + \overline{w}\partial z T') - (u'\partial x T' + v'\partial y T' + w'\partial z T') + R'.$$

The NDH can be defined as follows:

$$\text{NDH} = -(u'\partial x T' + v'\partial y T' + w'\partial z T'),$$

where T', u', v', and w' are temperature and zonal, meridional, and vertical velocity anomalies, respectively. Figure 5 gives the time-mean NDH differences between simulations with ENSO (WSA) and without ENSO (control) during the four seasons. The spatial features in NDH in the eastern equatorial Pacific and temperature differences in Fig. 4 are again found in agreement. For example, the positive NDH in the subsurface generally corresponds to temperature increases. The strongest positive NDH area located at 100°–80°W and 30–60 m in MAM also has a correspondence with the strongest temperature increases in Fig. 4; meanwhile, the second strongest temperature changes and NDH occur during DJF. However, the negative NDH in the western Pacific could not illustrate the cooling phenomenon in Fig. 4,
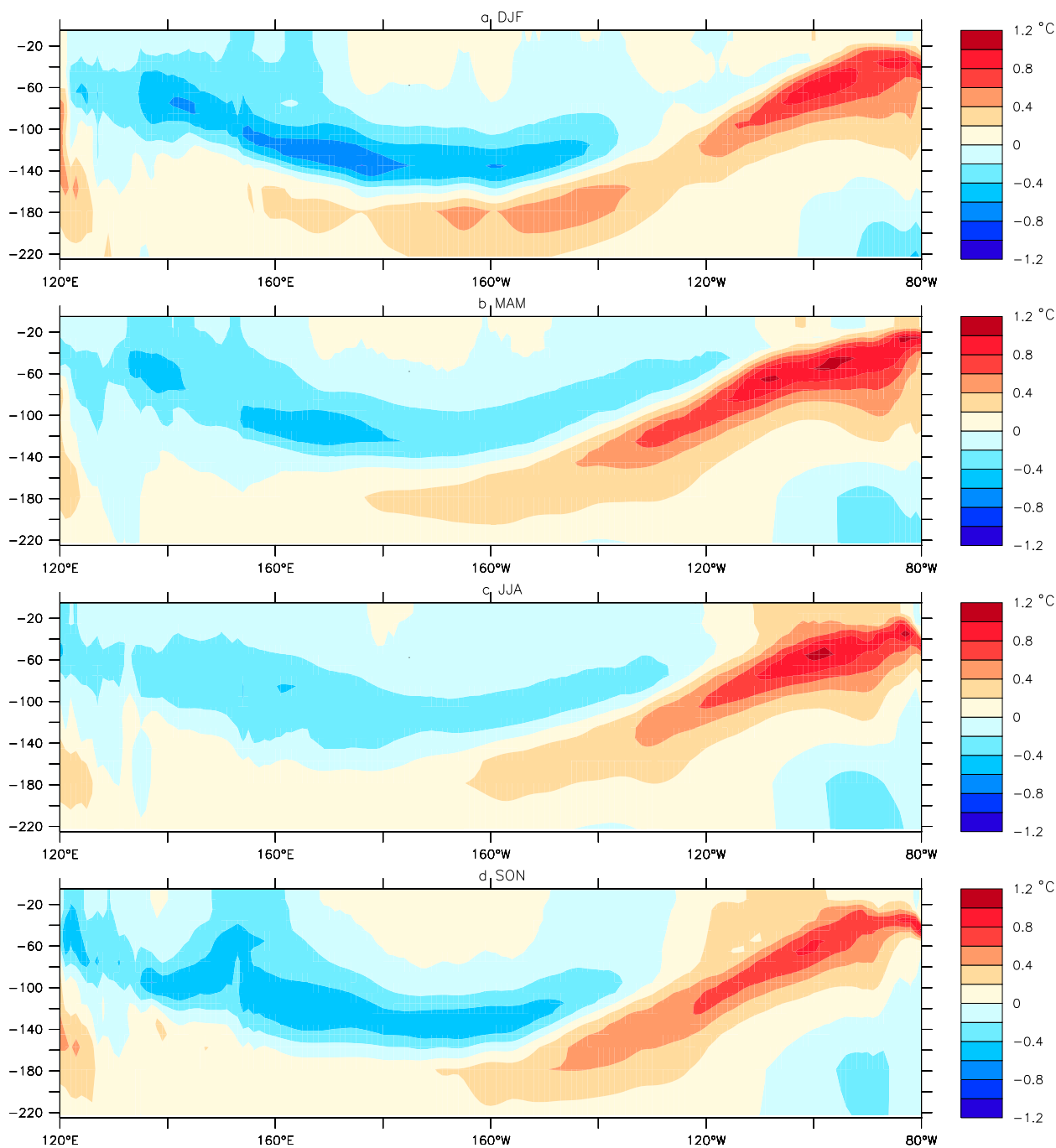
FIG. 4. Difference in the time-mean equatorial upper-ocean temperature for the four seasons as a function of depth and longitude between the runs with ENSO (WSA) and without ENSO (control).

because the cooling center in Fig. 4 corresponds to the positive NDH in Fig. 5; probably implying that NDH does not contribute to the cooling in the western equatorial Pacific.

Figure S6 in the supplementary material then considers the surface features during different seasons. Comparing Figs. S6 and S5, there is a significant correlation between them, especially near the equator. Furthermore, the seasonal variability is identical: the strongest positive NDH in the eastern Pacific including the eastern boundary occurs in JJA, whereas the most dramatic negative NDH in the western with the positive NDH in the central Pacific arise in SON.
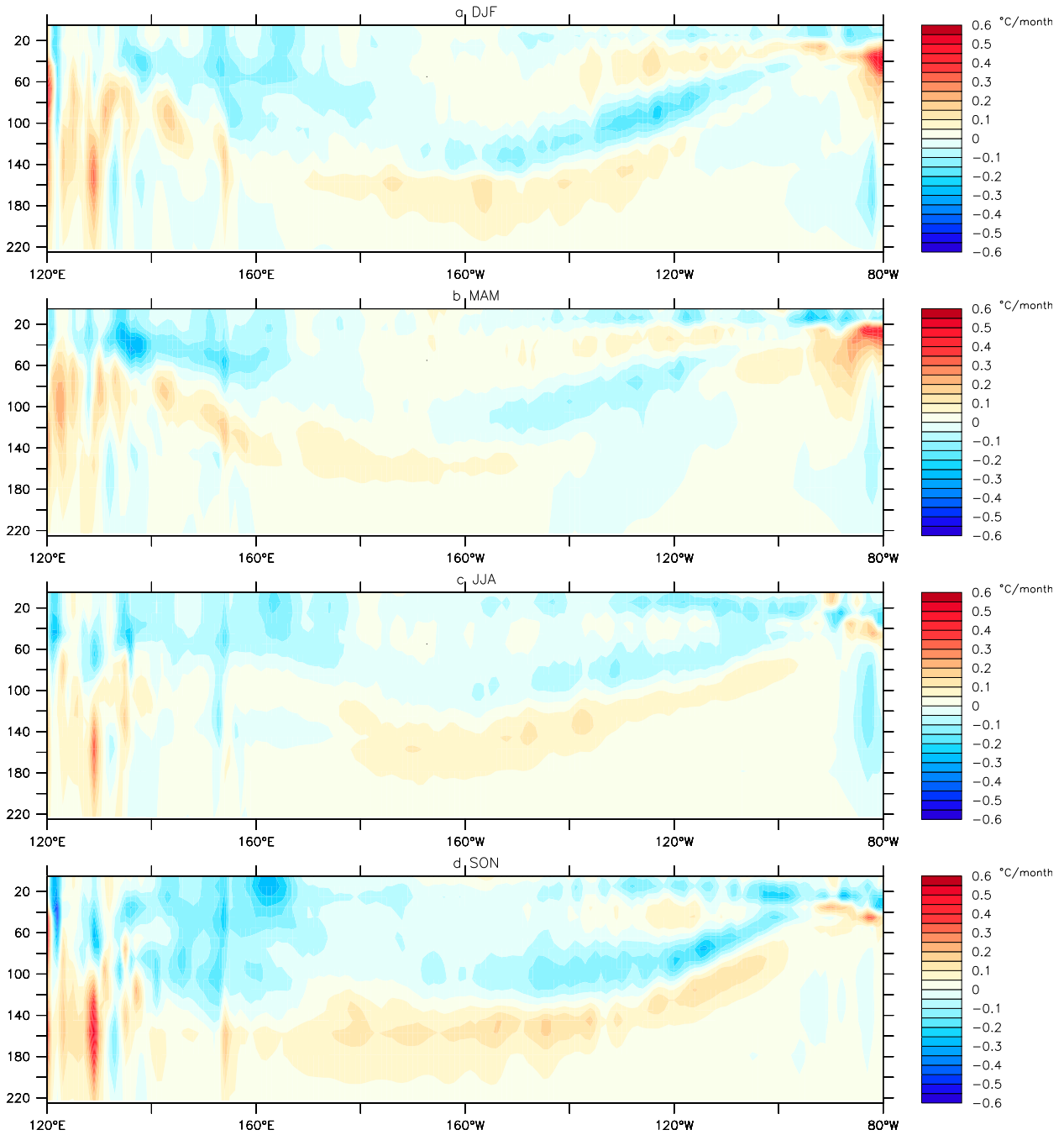
FIG. 5. Time-mean NDH difference for the four seasons as function of depth and longitude along equator between the runs with ENSO (WSA) and without ENSO (control).

2) SIMULATIONS FROM WSA_R

To better understand the mechanisms behind the rectified effect of ENSO onto the mean state, in particular, to show that the skewness in the wind stress anomalies applied does not really play a significant role, we have conducted another sensitivity experiment, WSA_R, and compared the rectification in this experiment with that in WSA. The wind stress anomalies are the same as in WSA, but their signs are reversed in WSA_R. This means that the forcing skewness is opposite between these two experiments. Surprisingly, we find that temperature (Fig. 6a) and SST (Fig. 6b) differences between WSA_R and the
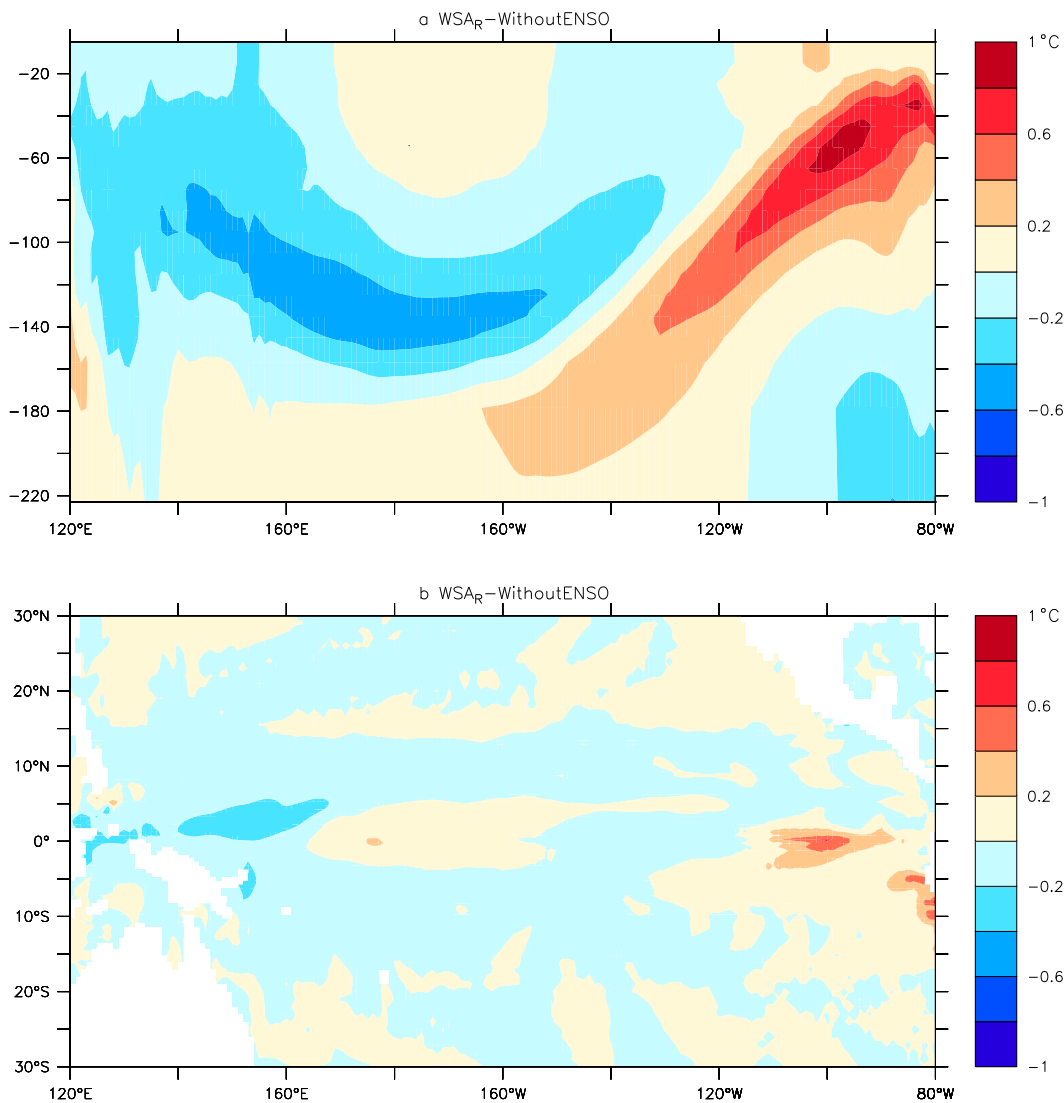
FIG. 6. As in Fig. 3, but for the WSA_R run in which the sign of the wind anomalies is reversed.

control run are highly similar to the corresponding differences between WSA and the control run (cf. Fig. 6 with Fig. 3). In other words, even though the external forcing skewness is reversed, the time-mean effect of ENSO remains unchanged, which underscores the singular importance of the nonlinear dynamical process in the upper ocean in rectifying the ENSO into the mean state. There are some noticeable differences, to be sure. For example, temperature cooling in the western equatorial Pacific appears to be more pronounced in WSA_R than in WSA. The temperature warming in the eastern Pacific in WSA extends farther to west than WSA_R (180° versus 160°W). In addition, it is noted that the warming to the SST in the eastern equatorial Pacific is larger in WSA than in WSA_R.

NDH differences between both WSA and WSA_R and the control run are shown in Fig. 7. The calculation of NDH was carried out offline using saved monthly output for temperature and current velocities. The major pattern in WSA_R resembles that in WSA. There are also noticeable differences. These differences include stronger heating in the central Pacific at 180°–140°W and 140–200 m in WSA_R, and the stronger negative NDH in 130°E–180° and 0–60 m in WSA_R. Comparing Fig. 7a with NDH in SZ2014 (Fig. 8), the features in the eastern and western equatorial Pacific are identical, but there is the negative characteristic in the central region near the surface at 180°–100°W and 0–20 m while this region has positive NDH in SZ2014. The negative NDH between 160° and 100°W at 60–120 m in our model also appears to be more profound.
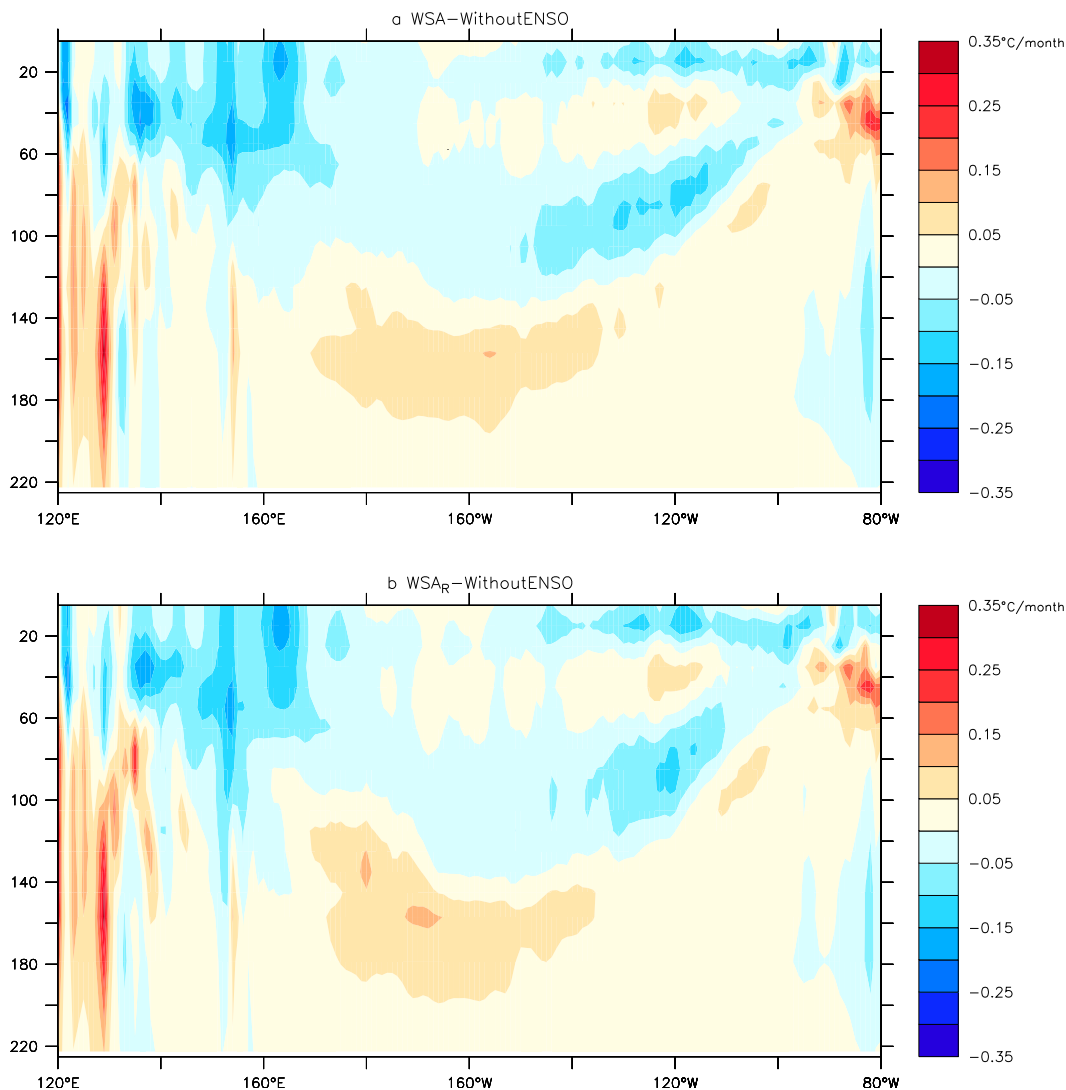
FIG. 7. Time-mean NDH difference as function of depth and longitude along the equator (a) between the runs with ENSO (WSA) and without ENSO and (b) between the runs with reversed ENSO (WSA_R) and without ENSO. Presented are the annual means (°C month^{-1}).

Figure 8 further shows the surface NDH differences. Just as shown in Fig. 7, the overall patterns in WSA and WSA_R are almost identical. The positive NDH in the eastern Pacific along the equator as well as the central Pacific along 5°N, however, appears to be stronger in WSA_R. In addition, the negative NDH over the warm pool is more profound in WSA_R too. The main features of the NDH pattern in WSA is consistent with SZ2014, with the exception of the regions 0°–5°N, 90°W and 0°–5°S, 160°–120°W, the present run has positive NDH while SZ2014 has negative NDH. Although there are differences between our results and those reported in SZ2014, the regions that have the strongest rectification signal agree well between these two models.

Figures 9 and 10 further show the three components of the total NDH presented in Figs. 7 and 8, respectively. There is a close resemblance between the zonal component of the NDH and the total NDH, which means that the total NDH shown in Figs. 7 and 8 mostly resulted from its zonal component: the advection of the temperature anomalies by the zonal current anomalies. The magnitudes of the meridional and vertical components of the NDH in Fig. 9 are also large, which shows the same importance as the zonal component, but in the subsurface they cancel each other. Thus, the most important contributor is the zonal component. However, in Fig. 10 the meridional and vertical components of the NDH do not cancel each other in the surface. The
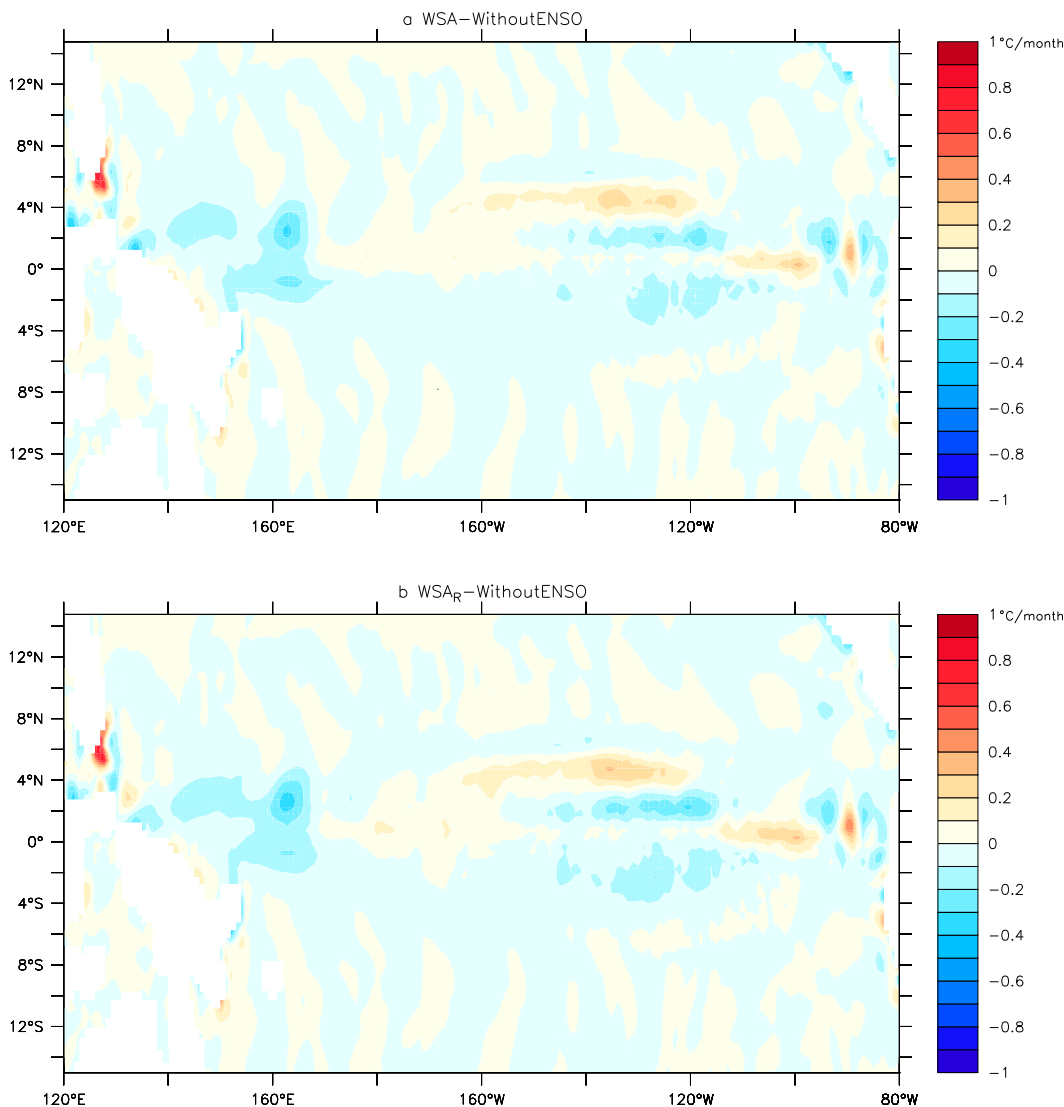
FIG. 8. Time-mean NDH difference for the surface layer as function of latitude and longitude (a) between the runs with ENSO (WSA) and without ENSO and (b) between the runs with reversed ENSO (WSA_R) and without ENSO. Presented are the annual-mean values (°C month^{-1}).

meridional component of the NDH in the surface also contributes significantly. All the above results agree with SZ2014. The differences only exist in the details. The negative meridional component is found at 160°–80°W and 0–20 m in Fig. 9, but it is positive in SZ2014. The negative meridional component in the region 3° south of the equator in Fig. 10 and the negative vertical component in the equator in Fig. 10 are different from SZ2014.

Figures 11 and 12 help to explain the positive NDH in the eastern equatorial Pacific. Fig. 11 shows the temperature anomalies superimposed by current anomalies averaged in 5°N–5°S, whereas Fig. 12 presents the same quantities averaged in 100°–80°W for El Niño and La

Niño events. Clearly, the warm phase pattern of WSA is almost identical to the cold phase pattern of WSA_R, while the cold phase pattern of WSA is almost identical to the warm phase of WSA_R, suggesting that the anomalous responses in both the temperature and currents are linear. From Fig. 11, we found that in the warm phase, in the subsurface of eastern equatorial Pacific at 100°–80°W, for $\partial xT' < 0$ and $u' > 0$, so $-u'\partial xT' > 0$, and for $\partial zT' < 0$ and $w' < 0$, so $-w'\partial zT' < 0$. While in the cold phase for $\partial xT' > 0$ and $u' < 0$, so $-u'\partial xT' > 0$, and for $\partial zT' > 0$ and $w' > 0$, so $-w'\partial zT' < 0$. Figure 12 elaborates the meridional component of the total NDH $-v'\partial yT' > 0$ in the warm and cold phases. In conclusion, the zonal and meridional components of the total NDH play a vital role in
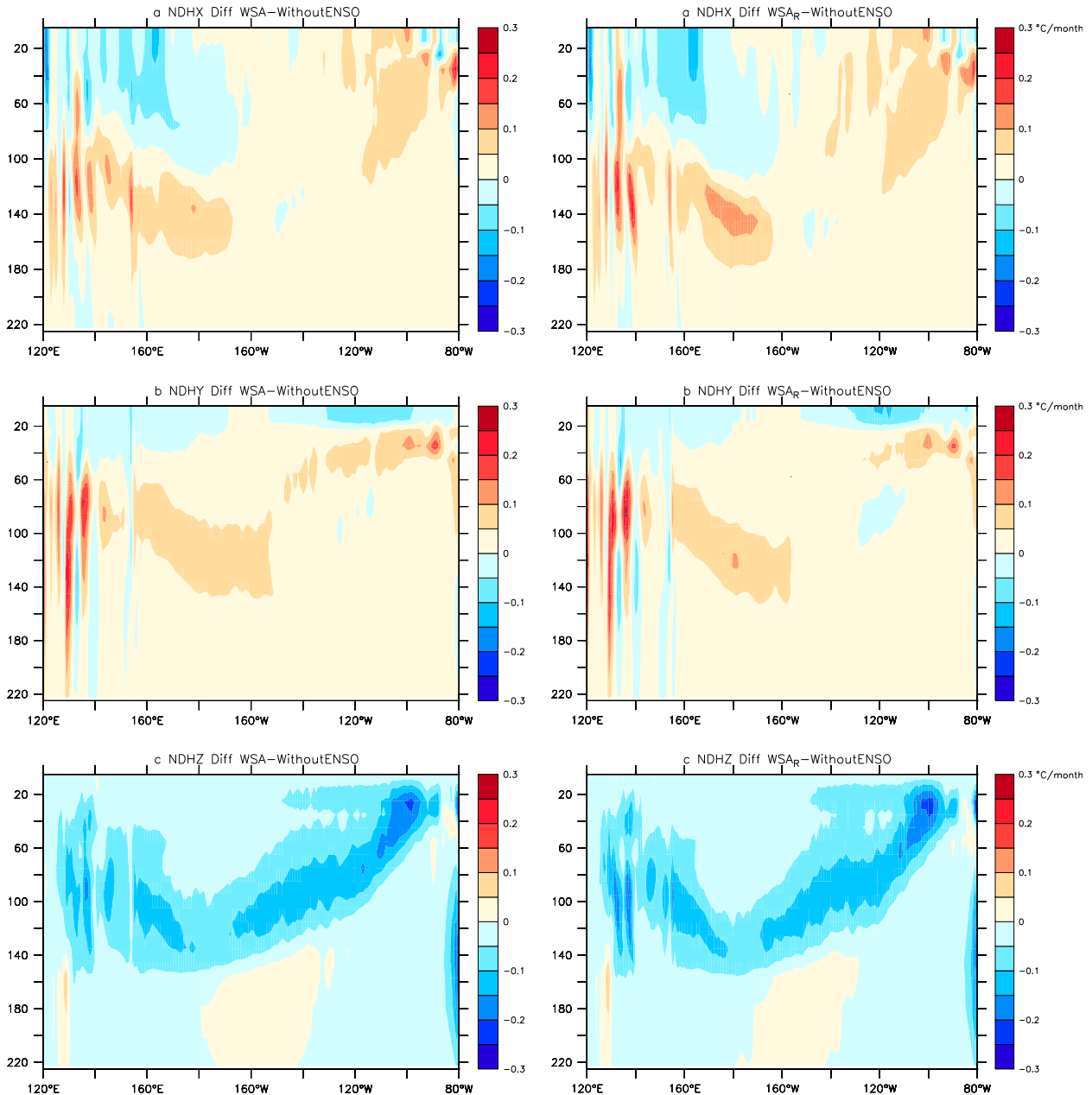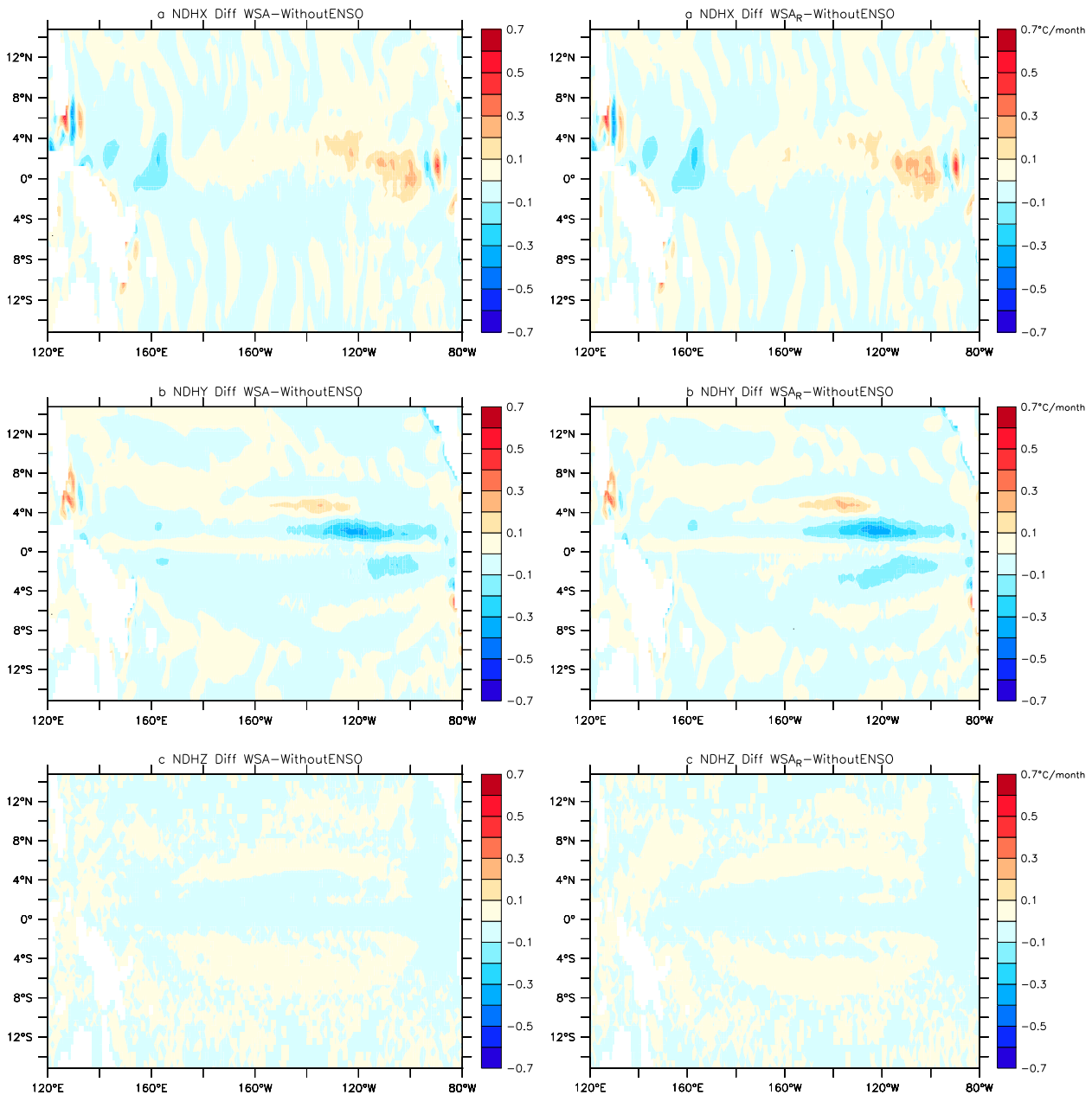
FIG. 9. As in Fig. 7, but for (a)–(c) the three components of the NDH (°C month^{-1}) for (left) WSA and (right) WSA_R (see text for more details).

inducing temperature increasing in the eastern equatorial Pacific, while the vertical component has the opposite contribution to the strongest positive NDH region; the results appear to be consistent with those in Su et al. (2010). The isopycnals in Figs. 11 and 12 show the corresponding density range in the two phases of ENSO. The heating is from dynamics, and it is adiabatic.

Why are the rectified effects of interannual fluctuations revealed in WSA and WSA_R largely the same?

Figures 13 and 14 help to answer this question. The features of annual-mean $\overline{u'T'}$, $\overline{v'T'}$, and $\overline{w'T'}$ components are shown in Fig. 13; just as before, WSA and WSA_R have high similarity, except for some small differences in magnitude in some regions, such as 180°–160°W and 120–160 m in Fig. 13a and 180°–140°W and 100–200 m in Fig. 13c. To understand the temperature and current anomalies specifically, we further present in Fig. 14 the time series of u', v', w', and T' averaged over

FIG. 10. As in Fig. 8, but for (a)–(c) the three components of the NDH (°C month^{-1}) for (left) WSA and (right) WSA_R.

the "action centers" shown in Fig. 13 (where $u'T'$, $v'T'$, and $w'T'$ have their respective maximum values). The temporal variability of u', v', w', and T' clearly shows the time series in WSA and WSA_R is almost opposite; it means that the u', v', w', and T' responses to the wind stress anomalies are linear, and when we multiply one item by another, the results in WSA and WSA_R would be identical. However, the magnitude is not exactly symmetric: in particular, the magnitude in the strongest El Niño years 1997/98 and 1982/83 is noticeably asymmetric and the magnitude asymmetry leads to the

corresponding magnitude discrepancies between WSA and WSA_R in Fig. 13 for these two strongest events.

4. Conclusions

Modeling studies and analyses of observations reveal a close relationship between ENSO variability and the mean state (e.g., Rodgers et al. 2004; Liang et al. 2012; SZ2014; Ogata et al. 2013). To unveil the physical mechanism behind this relationship, we have conducted forced ocean experiments to further study the
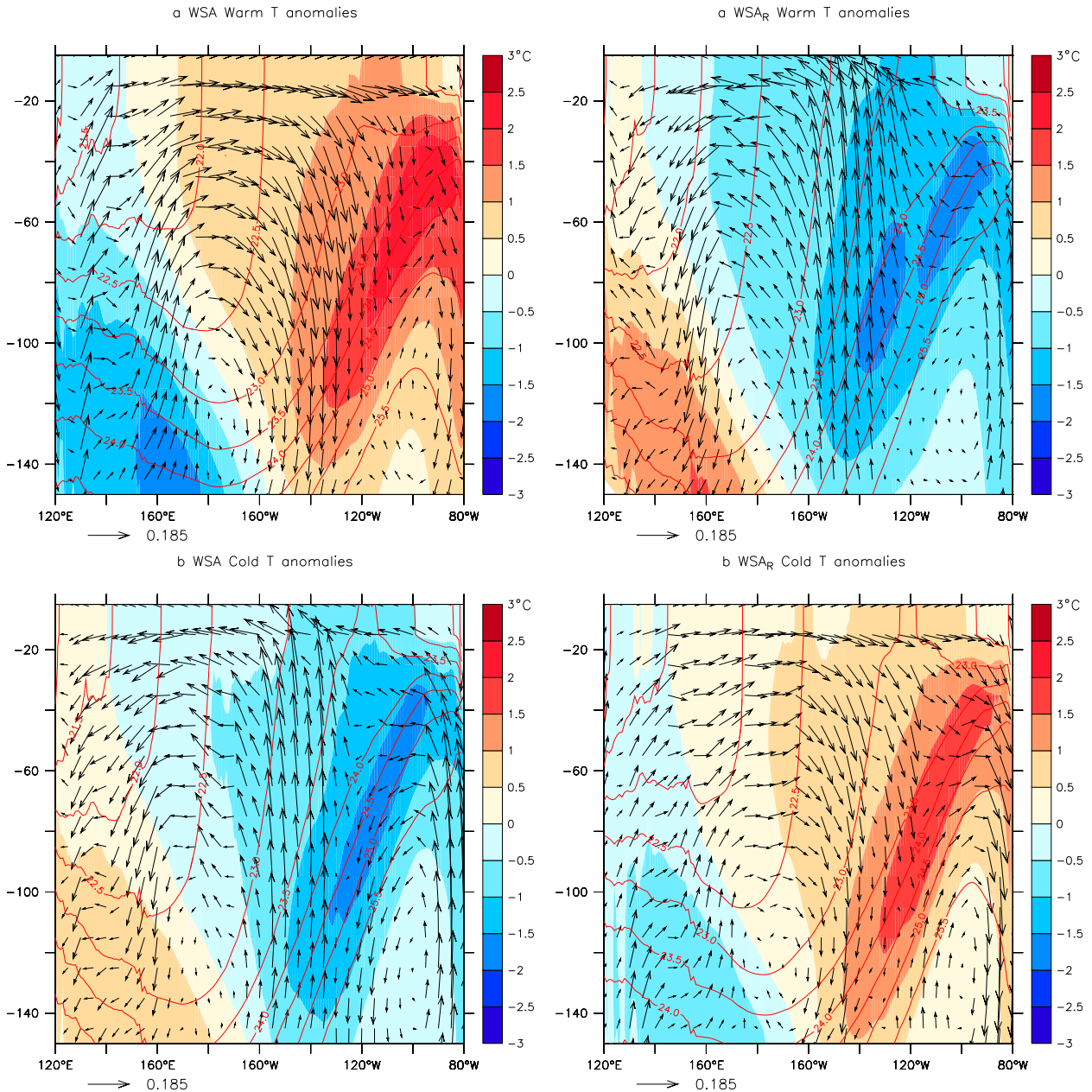
FIG. 11. Temperature anomalies along the equator (5°N–5°S) (contours) and the corresponding composite current anomalies (arrows) for (a) the warm phase and (b) the cold phase in (left) the WSA and (right) the WSA_R. Units for u' and w' are m s^{-1} and 10^5 m s^{-1}, respectively. The contours are the corresponding isopycnals (kg m^{-3}).

rectification effect of ENSO on the mean state. The basic methodology follows that of SZ2014, but a different ocean GCM is employed, allowing us to gauge model dependence of the results found in that study. Also, at least in one important aspect, the present GCM is more sophisticated than the model used in SZ2014: the present model has a seasonal cycle. More importantly, we note that the study of SZ2014 does not explicitly address the role of the asymmetry of wind anomalies in their

forced ocean experiments. Although their basic conclusion about the critical role of nonlinear ocean dynamics will not be affected as the long-term-mean wind stress in their two experiments is kept identical. Nonetheless, the curiosity remains about the role of the asymmetry already in the wind stress anomalies applied. So we report here an experiment that SZ2014 left out. In such an experiment, the wind stress anomalies are reversed in sign. Such an experiment turns out to be
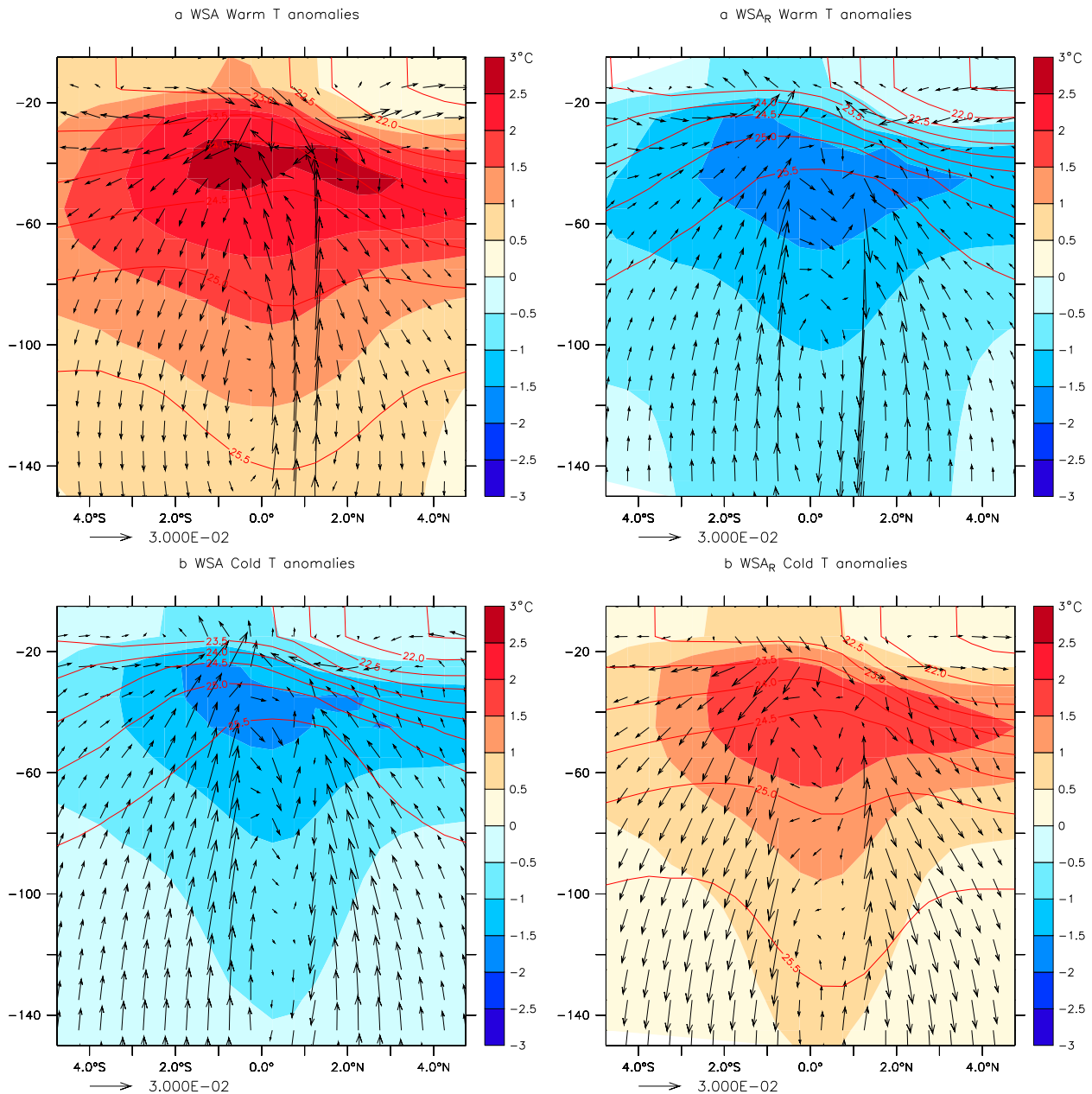
FIG. 12. Temperature anomalies averaged in the eastern Pacific Ocean (100°–80°W) and the corresponding current anomalies for (a) the warm phase and (b) the cold phase in (left) the WSA and (right) the WSA_R. Units for v' and w' are m s^{-1} and 10^4 m s^{-1}, respectively. The contours are the corresponding isopycnals (kg m^{-3}).

helpful in deepening our understanding the role of nonlinear upper-ocean dynamics in addition to showing explicitly that the asymmetry or skewness in the wind anomalies plays no role in the rectification, as originally anticipated in SZ2014.

The major result is that the major features found in SZ2014 about the rectified effect of ENSO do not depend on the model or have strong seasonal dependence. Our additional experiments—especially the experiment

in which the wind anomalies are reversed in sign— nonetheless shed more light on the mechanisms behind the rectification. The responses of the temperature and the current in the equatorial upper ocean are both very linear, leading their product to have a single sign. It is speculated that the linear response may have something to do with the strongly asymmetric state in the mean, but further studies are needed to further address this question.
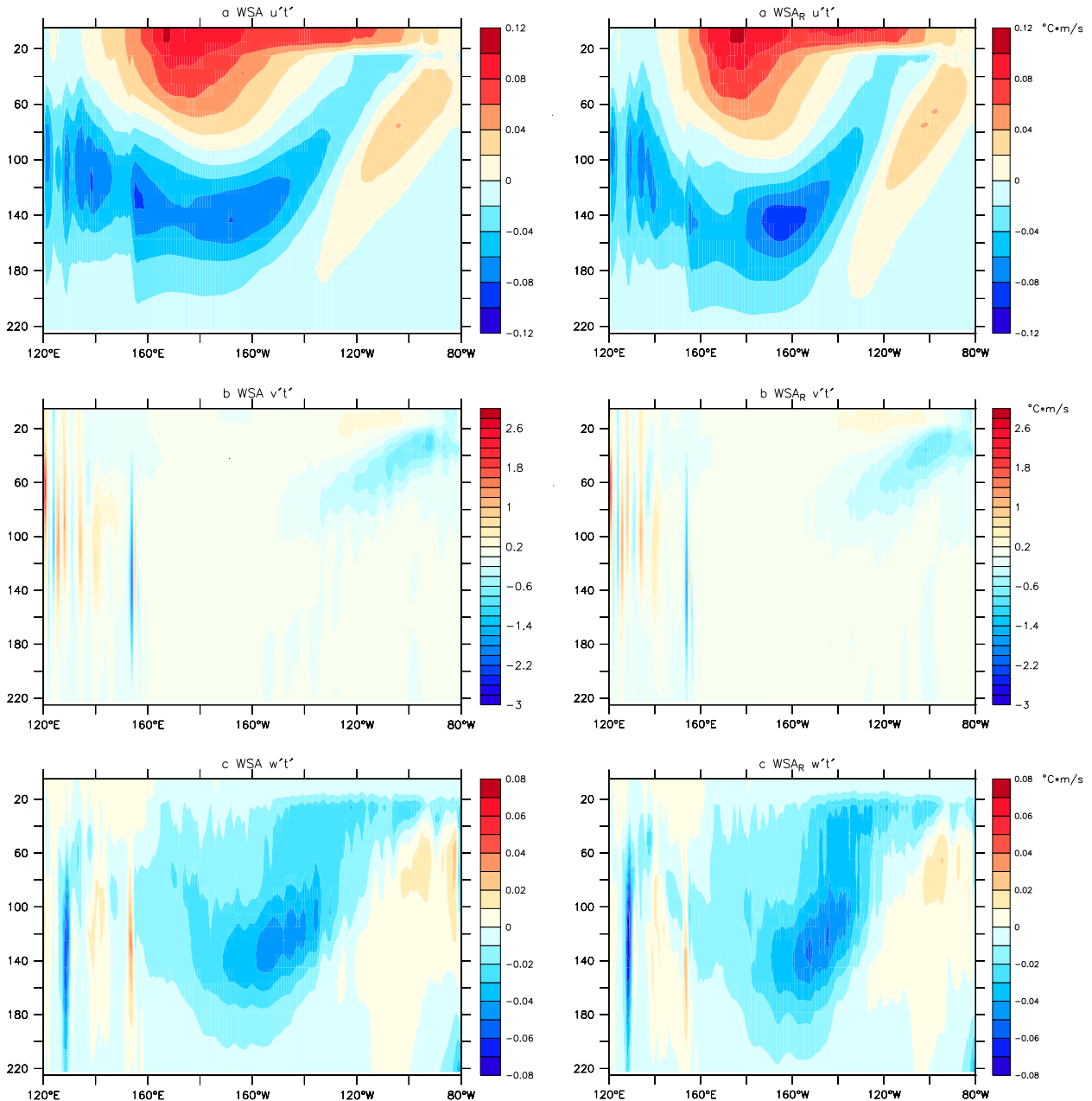
FIG. 13. The (a) $u'T'$, (b) $v'T'$, and (c) $w'T'$ runs (°C m s^{-1}) in the equatorial upper ocean (5°N–5°S), in (left) WSA and (right) WSA_R. We have scaled the w' by H/Lx, where Lx is half-width of the tropical Pacific and H is the depth of upper ocean (400 m), and v' by Ly/Lx, where Ly is the Rossby deformation radius on an equatorial beta plane.

There are also some details in the spatial pattern of the rectification that we want to pursue as future studies. The NDH cannot entirely account for the rectified effect. For example, the cooling in the equatorial far western Pacific is probably not connected with NDH. SZ2014 also noted a role of tropical instability waves. The present model has too course of a spatial resolution to capture this effect, which may explain some differences between the present results

and those reported in SZ2014. It is worth studying the effect of an increase in the resolution of the present ocean model (so that it can better represent the tropical instability waves; Jochum and Murtugudde 2004, 2006) on the rectification of ENSO. In addition, instead of using a restoring boundary condition, we may force the ocean GCM directly with fluxes from the atmosphere (Seager et al. 1995; Murtugudde et al. 1996; Deremble et al. 2013). Other possible factors
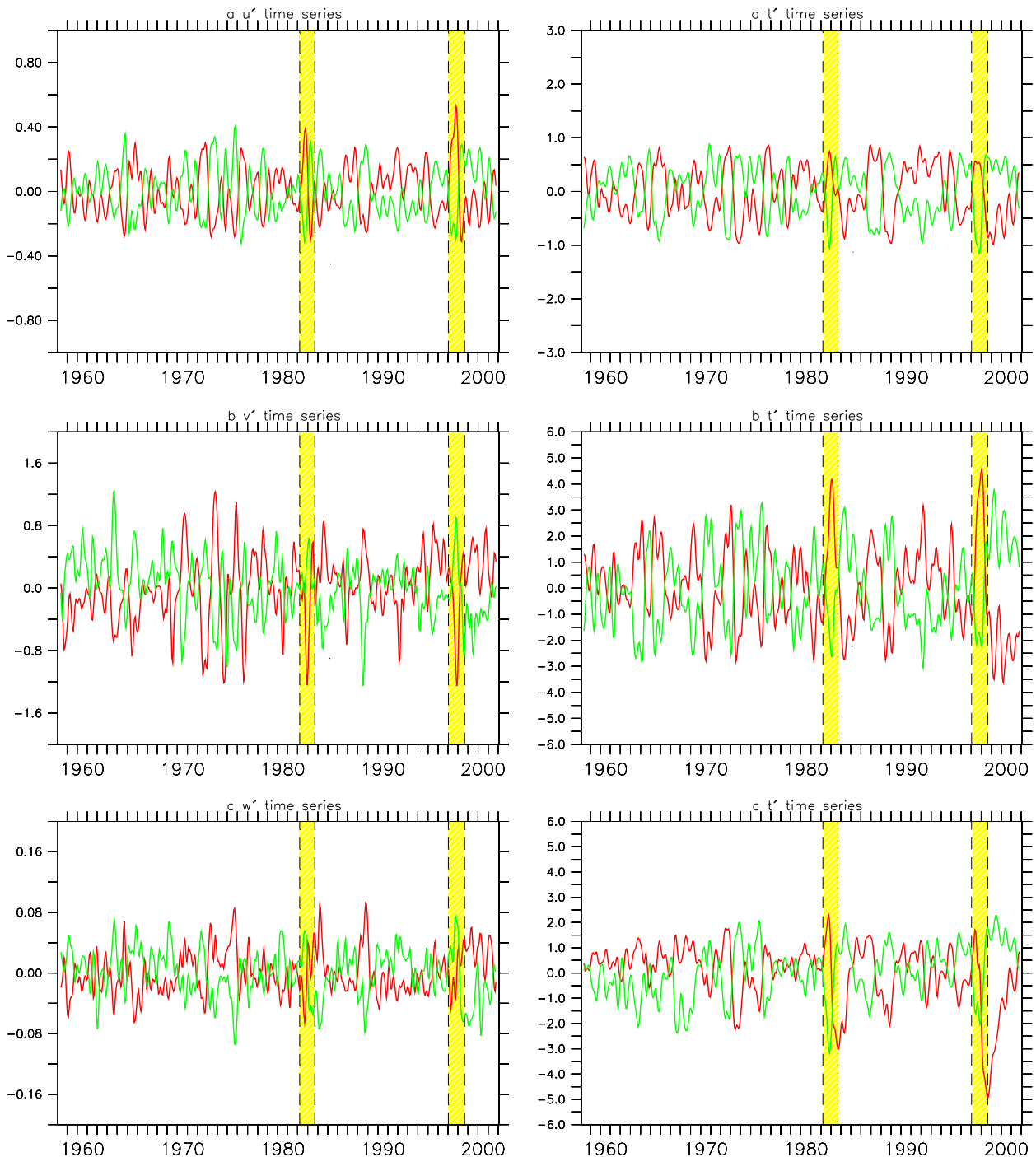
FIG. 14. (a) Time series of u' and T' averaged over the region (5°N–5°S, 170°E) at 20 m; (b) time series v' and T' averaged over the region (5°N–5°S, 95°W) at 30 m; and (c) w' and T' averaged over the region (5°N–5°S, 160°W) at 120 m for WSA (red line) and WSA_R (green line). Yellow shading represents significant El Niño events. We select the regions for which Fig. 13 has the corresponding maximum values for $u'T'$, $v'T'$, and $w'T'$. As in Fig. 13, we have scaled w' by H/Lx and v' by Ly/Lx.

that may be included in the future investigations are asymmetric anomalies of atmospheric circulation (Wu et al. 2010) and the biogeochemistry process (Timmermann and Jin 2002).

REFERENCES

An, S. I., 2008: Interannual variations of the tropical ocean instability wave and ENSO. *J. Climate,* **21,** 3680–3686, doi:10.1175/2008JCLI1701.1.

——, and F. F. Jin, 2004: Nonlinearity and asymmetry of ENSO. *J. Climate,* **17,** 2399–2412, doi:10.1175/1520-0442(2004)017<2399: NAAOE>2.0.CO;2.

Battisti, D. S., and A. C. Hirst, 1989: Interannual variability in a tropical atmosphere–ocean model: Influence of the basic state, ocean geometry, and nonlinearity. *J. Atmos. Sci.,* **46,** 1687–1712, doi:10.1175/1520-0469(1989)046<1687:IVIATA>2.0.CO;2.

Bjerknes, J., 1969: Atmospheric teleconnections from the equatorial Pacific. *Mon. Wea. Rev.,* **97,** 163–172, doi:10.1175/1520-0493(1969)097<0163:ATFTEP>2.3.CO;2.

Canuto, V. M., and M. S. Dubovikov, 2005: Modeling mesoscale eddies. *Ocean Modell.,* **8,** 1–30, doi:10.1016/j.ocemod.2003.11.003.

Carton, J. A., and B. S. Giese, 2008: A reanalysis of ocean climate using Simple Ocean Data Assimilation (SODA). *Mon. Wea. Rev.,* **136,** 2999–3017, doi:10.1175/2007MWR1978.1.

Delworth, T. L., and Coauthors, 2006: GFDL's CM2 global coupled climate models. Part I: Formulation and simulation characteristics. *J. Climate,* **19,** 643–674, doi:10.1175/JCLI3629.1.

Deremble, B., N. Wienders, and W. K. Dewar, 2013: CheapAML: A simple, atmospheric boundary layer model for use in ocean-only model calculations. *Mon. Wea. Rev.,* **141,** 809–821, doi:10.1175/MWR-D-11-00254.1.

Gent, P. R., and M. A. Cane, 1989: A reduced gravity, primitive equation model of the upper equatorial ocean. *Comput. Phys.,* **81,** 444–480, doi:10.1016/0021-9991(89)90216-7.

——, and J. C. McWilliams, 1990: Isopycnal mixing in ocean circulation models. *J. Phys. Oceanogr.,* **20,** 150–155, doi:10.1175/1520-0485(1990)020<0150:IMIOCM>2.0.CO;2.

Gibson, J. K., P. Kallberg, S. Uppala, A. Hernandez, A. Normuram, and E. Serrano, 1997: ERA description. ECMWF Re-Analysis Project Rep., 72 pp.

Jin, F. F., 1997: An equatorial ocean recharge paradigm for ENSO. Part I: Conceptual model. *J. Atmos. Sci.,* **54,** 811–829, doi:10.1175/1520-0469(1997)054<0811:AEORPF>2.0.CO;2.

——, S. I. An, A. Timmermann, and J. X. Zhao, 2003: Strong El Niño events and nonlinear dynamical heating. *Geophys. Res. Lett.,* **30,** 1120, doi:10.1029/2002GL016356.

Jochum, M., and R. Murtugudde, 2004: Internal variability in the tropical Pacific Ocean. *Geophys. Res. Lett.,* **31,** L14309, doi:10.1029/2004GL020488.

——, and ——, 2006: Temperature advection by tropical instability waves. *J. Phys. Oceanogr.,* **36,** 592–605, doi:10.1175/JPO2870.1.

Kosaka, Y., and S. P. Xie, 2013: Recent global-warming hiatus tied equatorial Pacific surface cooling. *Nature,* **501,** 403–407, doi:10.1038/nature12534.

Large, W. G., G. Danabasoglu, S. C. Doney, and J. C. McWilliams, 1997: Sensitivity to surface forcing and boundary layer mixing in a global ocean model: Annual-mean climatology. *J. Phys.*

Oceanogr., **27,** 2418–2447, doi:10.1175/1520-0485(1997)027<2418: STSFAB>2.0.CO;2.

Levitus, S., and T. P. Boyer, 1994: *Temperature.* Vol. 4, *World Ocean Atlas 1994,* NOAA Atlas NESDIS 4, 117 pp.

——, R. Burgett, and T. P. Boyer, 1994: *Salinity.* Vol. 3, *World Ocean Atlas 1994,* NOAA Atlas NESDIS 3, 99 pp.

Liang, J., X. Q. Yang, and D. Z. Sun, 2012: The effect of ENSO events on the tropical Pacific mean climate: Insights from an analytical model. *J. Climate,* **25,** 7590–7606, doi:10.1175/JCLI-D-11-00490.1.

Liu, H. L., X. Zhang, W. Li, Y. Yu, and R. Yu, 2004a: An eddy-permitting oceanic general circulation model and its preliminary evaluation. *Adv. Atmos. Sci.,* **21,** 675–290, doi:10.1007/BF02916365.

——, ——, Y. Yu, and W. Li, 2004b: *Manual for LASG/IAP Climate System Ocean Model* (in Chinese). Science Press, 108 pp.

——, P. F. Lin, Y. Q. Yu, and X. H. Zhang, 2012: The baseline evaluation of LASG/IAP climate system ocean model (LICOM) version 2. *Acta Meteor. Sin.,* **26,** 318–329, doi:10.1007/s13351-012-0305-y.

Locarnini, R. A., A. V. Mishonov, J. I. Antonov, T. P. Boyer, and H. E. Garcia, 2010: *Temperature.* Vol. 1, *World Ocean Atlas 2009,* NOAA Atlas NESDIS 68, 184 pp.

Meehl, G. A., A. Hu, J. M. Arblaster, J. Fasullo, and K. E. Trenberth, 2013: Externally forced and internally generated decadal climate variability associated with the interdecadal Pacific oscillation. *J. Climate,* **26,** 7298–7310, doi:10.1175/JCLI-D-12-00548.1.

Murtugudde, R., R. Seager, and A. J. Busalacchi, 1996: Simulation of the tropical oceans with an ocean GCM coupled to an atmospheric mixed-layer model. *J. Climate,* **9,** 1795–1815, doi:10.1175/1520-0442(1996)009<1795:SOTTOW>2.0.CO;2.

Ogata, T., S. P. Xie, A. Wittenberg, and D. Z. Sun, 2013: Interdecadal amplitude modulation of El Niño–Southern Oscillation and its impacts on tropical Pacific decadal variability. *J. Climate,* **26,** 7280–7297, doi:10.1175/JCLI-D-12-00415.1.

Rayner, N. A., D. E. Parker, E. B. Horton, C. K. Folland, L. V. Alexander, D. P. Rowell, E. C. Kent, and A. Kaplan, 2003: Global analyses of sea surface temperature, sea ice, and night marine air temperature since the late nineteenth century. *J. Geophys. Res.,* **108,** 4407, doi:10.1029/2002JD002670.

Rodgers, K. B., P. Friederichs, and M. Latif, 2004: Tropical Pacific decadal variability and its relation to decadal modulations of ENSO. *J. Climate,* **17,** 3761–3774, doi:10.1175/1520-0442(2004)017<3761:TPDVAI>2.0.CO;2.

Roeske, F., 2001: An atlas of surface flues based on the ECMWF reanalysis—A climatological dataset to force global ocean general circulation models. Max-Planck-Institut für Meteorologie Rep. 23, 31 pp.

Schopf, P. S., and R. J. Burgman, 2006: A simple mechanism for ENSO residuals and asymmetry. *J. Climate,* **19,** 3167–3179, doi:10.1175/JCLI3765.1.

Seager, R., M. Blumenthal, and Y. Kushnir, 1995: An advective atmospheric mixed layer model for ocean modeling purposes: Global simulation of surface heat fluxes. *J. Climate,* **8,** 1951–1964, doi:10.1175/1520-0442(1995)008<1951: AAAMLM>2.0.CO;2.

Su, J. Z., R. H. Zhang, T. Li, X. Rong, J. S. Kug, and C. C. Hong, 2010: Causes of the El Niño and La Niña amplitude asymmetry in the equatorial eastern Pacific. *J. Climate,* **23,** 605–617, doi:10.1175/2009JCLI2894.1.

Suarez, M. J., and P. S. Schopf, 1988: A delayed action oscillator for ENSO. *J. Atmos. Sci.,* **53,** 2786–2802.

Sun, D. Z., 1997: El Niño: A coupled response to radiative heating? *Geophys. Res. Lett.,* **24,** 2031–2034, doi:10.1029/97GL01960.

——, 2003: A possible effect of an increase in the warm-pool SST on the magnitude of El Niño warming. *J. Climate,* **16,** 185–205, doi:10.1175/1520-0442(2003)016<0185:APEOAI>2.0.CO;2.

——, and T. Zhang, 2006: A regulatory effect of ENSO on the time-mean thermal stratification of the equatorial upper ocean. *Geophys. Res. Lett.,* **33,** L07710, doi:10.1029/2005GL025384.

——, ——, and S. I. Shin, 2004: The effect of subtropical cooling on the amplitude of ENSO: A numerical study. *J. Climate,* **17,** 3786–3798, doi:10.1175/1520-0442(2004)017<3786:TEOSCO>2.0.CO;2.

——, Y. Yu, and T. Zhang, 2009: Tropical water vapor and cloud feedbacks in climate models: A further assessment using coupled simulations. *J. Climate,* **22,** 1287–1304, doi:10.1175/2008JCLI2267.1.

——, T. Zhang, S. Yan, and Y. Yu, 2014: Rectification of El Niño–Southern Oscillation into climate anomalies of longer time-scales: Results from forced ocean GCM experiments. *J. Climate,* **27,** 2545–2561, doi:10.1175/JCLI-D-13-00390.1.

Sun, F. P., and J. Y. Yu, 2009: A 10–15-yr modulation cycle of ENSO intensity. *J. Climate,* **22,** 1718–1735, doi:10.1175/2008JCLI2285.1.

Timmermann, A., and F. F. Jin, 2002: Phytoplankton influences on tropical climate. *Geophys. Res. Lett.,* **29,** 2104, doi:10.1029/2002GL015434.

Uppala, S. M., and Coauthors, 2005: The ERA-40 Re-Analysis. *Quart. J. Roy. Meteor. Soc.,* **131,** 2961–3012, doi:10.1256/qj.04.176.

Wittenberg, A. T., 2009: Are historical records sufficient to constrain ENSO simulations? *Geophys. Res. Lett.,* **36,** L12702, doi:10.1029/2009GL038710.

Wu, B., T. Li, and T. Zhou, 2010: Asymmetry of atmospheric circulation anomalies over the western North Pacific between El Niño and La Niña. *J. Climate,* **23,** 4807–4821, doi:10.1175/2010JCLI3222.1.

Yu, J. Y., and S. T. Kim, 2011: Reversed spatial asymmetries between El Niño and La Niño and their linkage to decadal ENSO modulation in CMIP3 models. *J. Climate,* **24,** 5423–5434, doi:10.1175/JCLI-D-11-00024.1.

Yu, Y. Q., and D. Z. Sun, 2009: Response of ENSO and the mean state of the tropical Pacific to extratropical cooling/warming: A study using the IAP coupled model. *J. Climate,* **22,** 5902–5917, doi:10.1175/2009JCLI2902.1.

——, W. P. Zheng, H. L. Liu, and X. H. Zhang, 2007: The LASG Coupled Climate System Model FGCM-1.0 (in Chinese). *Chin. J. Geophys.,* **50,** 1677–1687.

——, H. Zhi, B. Wang, H. Wan, H. L. Liu, W. Li, W. P. Zheng, and T. Zhou, 2008: Coupled model simulations of climate changes in the 20th century and beyond. *Adv. Atmos. Sci.,* **25,** 641–654, doi:10.1007/s00376-008-0641-0.

——, W. Zheng, B. Wang, H. Liu, and J. Liu, 2011: Versions g1.0 and g1.1 of the LASG/IAP Flexible Global Ocean-Atmosphere-Land System model. *Adv. Atmos. Sci.,* **28,** 99–117, doi:10.1007/s00376-010-9112-5.